Nanoscale

Accepted Manuscript

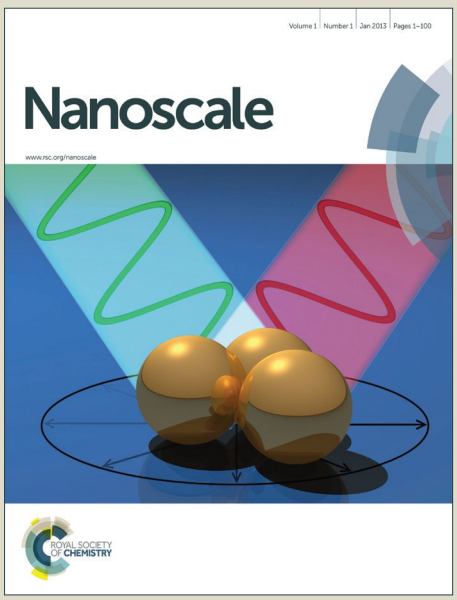

ROYAL SOCIETY OF CHEMISTRY

www.rsc.org/nanoscale

Nanoscale

ARTICLE

Nanogenerators Based on Vertically Aligned InN Nanowires

Guocheng Liu,*[a] Songrui Zhao,[b] Robert D. E. Henderson,[c] Zoya Leonenko,[c] Eihab Abdel-Rahman,[d] Zetian Mi[b] and Dayan Ban*[a]

Piezoelectric nanogenerators (NGs) based on vertically aligned InN nanowires (NWs) are fabricated, characterized, and evaluated. In these NGs, arrays of *p*-type and intrinsic InN NWs prepared by plasma-assisted molecular beam epitaxy (MBE) demonstrate similar piezoelectric properties. The *p*-type NGs show 160% more output current and 70% more output power product than the intrinsic NGs. The features driving performance enhancement are reduced electrostatic losses due to better NW array morphology, improved electromechanical energy conversion efficiency due to smaller NW diameters, and the higher impedance of intrinsic NGs due to elevated NW surface charge levels. These findings highlight the potential of InN based NGs as a power source for self-powered systems and the importance of NW morphology and surface state on overall NG performance.

www.rsc.org/nanoscale

1. Introduction

Nanowire (NW) arrays' unique advantages, such as high surface area, relatively high flexibility, and sensitivity to small forces, make them ideal candidates for piezoelectric nanogenerator (NG) applications.[1-4] Under strain, the ions of crystals within the non-centrosymmetric wurtzite structures of semiconductors NWs, such as ZnO, GaN, InN, and CdS, become polarized and generate piezoelectric potential (piezopotential).[5] The NWs' simultaneous possession of piezoelectric and semiconductor properties strongly affects carrier transport at interfaces and junctions when piezopotential is created. Under external strain, NGs made of NW arrays produce a piezopotential, which is then balanced by a corresponding transient flow of electrons through an external load.[6]

NWs based on III-nitrides such as AlN, AlGaN, GaN, and InN are noted for their tunability, direct band gap, high chemical stability, and strong resistance to atmospheric moisture.[7, 8] Earlier research revealed that the piezopotential and piezoelectricity of these materials increase in the sequence AlN, AlGaN, GaN, and InN.[7] Due to their very poor conductivity, intrinsic AlN and AlGaN cannot produce electric output power upon the application of mechanical strain. In contrast, InN NWs demonstrate outstanding potential for piezoelectric energy generation, outperforming ZnO and GaN NWs'.[7, 9, 1] Furthermore, InN can be grown on Si substrates at low temperature, within the complementary metal-oxide semiconductor (CMOS) thermal budget, thereby enabling integration with Si CMOS technology. InN is also critically important for ternary III-nitride semiconductors, such as In(Ga)N-based devices,[11-21] which are being widely adopted by the semiconductor industry. Unlike arsenide and phosphide based materials, InN is environmentally friendly and much safer to use.

While, GaN-based devices and systems are relatively mature, indium-containing III-nitride devices remain underdeveloped, hampered by InN planar/bulk structural challenges, such as uncontrolled surface electron accumulation, and by difficulties in realizing *p*-type and intrinsic InN. The highly efficient strain and thermal relaxation in NW lateral surfaces can be used to substantially minimize the large dislocation density observed in InN planar structures grown on lattice-mismatched substrates.[22-24]

This paper investigates the use of InN NW arrays to develop piezoelectric NGs. It demonstrates for the first time NGs based on *p*-type and intrinsic InN NWs. A systematic study is carried out to compare the materials of *p*-type and intrinsic InN NWs, and the performance of piezoelectric NGs based upon them. Section 2 describes the fabrication and characterization of the NWs and NGs. Section 3 reports the results of those experiments. Section 4 analyzes the characteristics of *p*-type and intrinsic InN NWs and the performance of the NGs based on them, while section 5 concludes this paper.

2. Methods

2.1 InN NW Growth

[a] Department of Electrical and Computer Engineering, Waterloo Institute for Nanotechnology, University of Waterloo, 200 University Ave. West, Waterloo, Ontario, N2L3G1, Canada. E-mail: g37liu@uwaterloo.ca; dban@uwaterloo.ca
[b] Department of Electrical and Computer Engineering, McGill University, Montreal, Quebec, H3A 0E9, Canada
[c] Department of Physics & Astronomy, Waterloo Institute for Nanotechnology, University of Waterloo, Waterloo, Ontario, N2L 3G1, Canada
[d] Department of System Design Engineering, Waterloo Institute for Nanotechnology, University of Waterloo, Waterloo, Ontario, N2L 3G1, Canada
† Electronic Supplementary Information (ESI) available. See DOI:10.1039/

Using radio frequency plasma-assisted molecular beam epitaxy (MBE), magnesium (Mg)-doped (*p*-type) and nominally un-doped (intrinsic) InN NWs were grown on separate Si (111) substrates under nitrogen-rich conditions by means of the InN NW growth procedure detailed in [15, 19, 25]. A thin (~ 0.6 nm) indium seeding layer was deposited on Si substrates before introducing nitrogen. This layer forms nanoscale droplets at high temperature, enhancing subsequent nucleation and growth of InN NWs. The *p*-type and intrinsic InN NWs were grown at a substrate temperature of ~ 480 ℃, an indium beam equivalent pressure of ~ 6×10^{-8} Torr, a nitrogen flow rate of ~ 1.0 sccm, and RF plasma forward power of ~ 350 W. Under these optimized growth conditions, nominally un-doped InN nanowires are nearly intrinsic. To grow *p*-type InN NWs, a magnesium (Mg) cell was introduced into the chamber.

2.2 NW Characterization

The morphology and crystalline structure were investigated using a field-emission scanning electron microscope (FE-SEM, Zeiss) and a high resolution X-ray diffraction (XRD) system (Jordan Valley QC3). Raman spectroscopy was taken at room temperature, using a HeNe laser operating at a wavelength of 632 nm and power of 30 mW, with its focal spot tuned to a diameter of ~ 5 μm. The samples' electric and piezoelectric properties were investigated using conductive atomic force microscopy (C-AFM, SmartSPM™-1000, AIST-NT) with platinum/iridium (Pt/Ir) coated conductive tips (HQ: NSC14/Pt, MikroMasch) and a force constant of ~ 5 N/m. Kelvin probe force microscopy (KPFM) imaging was conducted using MikroMasch tips (HQ-NSC15/Pt) with a natural frequency of ~ 325 kHz and force constant of ~ 40 N/m. The examination was carried out in amplitude-modulation (AM) mode simultaneously with the topography, by scanning the lines twice (once for height and another for KPFM) at a setoff distance of 10 nm. AM-KPFM offers significantly enhanced resolution and sensitivity over the more traditional lift mode KPFM. The scan rates were kept low (0.5 – 1 Hz) for optimal image quality.

2.3 NG Fabrication

To fabricate the nanogenerators (NGs), an insulating layer made of polymethyl methacrylate (PMMA), MicroChem 950k A11, was spin-coated to encapsulate the NWs. The PMMA layer was then cured at 90 ℃ for 3 hours. The encapsulation protects the NWs from damage under mechanical strain and prevents electrical shorting between the NWs' electrodes.[26] It does not prevent the application of external strain to the NWs, due to the PMMA's compliance.[27] To increase the interfacial energy barrier and protect against the inconsistency of the PMMA polymer matrix, a thin (10 nm) molybdenum oxide (MoO_3) interlayer was deposited atop the PMMA polymer matrix by vacuum thermal evaporation, immediately followed by a 50 nm thick gold (Au) cathode layer to complete the devices. Silver paste was used to glue copper (Cu) wire leads to the bottom highly doped Si substrate and the top Au electrode. The completed NGs' area was 9×9 mm^2. They were encapsulated in polydimethylsiloxane (PDMS), Dow Corning Sylgard 184 premixed with curing agent at a ratio of 10:1 w/w and degassed, to prevent contamination, damage, and moisture penetration from the ambient environment.

2.4 NG Characterization

Characterizations of the fabricated InN NW-based piezoelectric NGs was performed using a close loop (Vibration Research Corporation, VR9500) electromagnetic shaker (Labworks Inc. ET-126B-1). The NGs output voltage and current signals were measured using Stanford low-noise voltage/current preamplifiers (Model SR560/570) and a National Instruments I/O module (NI CompactDAQ USB-9239). For voltage and current measurements, the input resistances of the preamplifiers were set to 100 MΩ (SR560) and 10 kΩ (SR570), respectively. To minimize electromagnetic interference, the copper wires connected to the NG leads were twisted together. All measurements were taken at ambient room temperature.

3. Results

Fig. 1 shows 45°-tilted SEM images of as-grown *p*-type and intrinsic InN NWs on a Si (111) substrate. The NWs exhibit a vertical surface morphology with a well-defined hexagonal cross-section and nearly perfect straight and smooth surfaces along the *c*-axis. The average *p*-type NW diameter and length were 400 nm and 1.0 μm, respectively, and the area density was 9×10^7 cm^{-2}. The average intrinsic NW (Fig. 1b) diameter and length were 500 nm and 0.7 μm, respectively, and the area density was 7×10^7 cm^{-2}. We define the NW aspect ratio α as the average NW length divided by the average NW diameter, and the fill ratio β as the average NW diameter divided by the average NW pitch. We observe that *p*-type InN NWs have higher aspect and fill ratios of $\alpha_p = 2.5$ and $\beta_p = 0.4$ than intrinsic NWs at $\alpha_i = 1.4$ and $\beta_i = 0.3$, which are consistent with the results published by Zhao *et al.* [19, 25]

Fig. 2 shows the 2θ-scan spectra of the XRD intensity for *p*-type and intrinsic NWs. The sharp peak at 31.4°, corresponding to the (002) plane, reveals the highly crystalline quality of the InN NWs and their *c*-axis preferred orientation. The full width at half-maximum (FWHM) of the θ-rocking curve of the (002) peak is 0.23° (Fig. 2, inset), demonstrating the NWs' excellent alignment. The intensity of the diffraction peak in the XRD 2θ scan of the *p*-type InN NWs is much stronger than that of the intrinsic NWs, confirming that incorporating Mg dopant enhances NW growth along the preferred direction.[25] The Raman spectrum of *p*-type InN NWs (Fig. S1†) exhibited a very narrow E_2^h phonon peak at 488 cm^{-1} (FWHM = 4 ± 0.1 cm^{-1}) and an A_1 (LO) phonon peak at 593 cm^{-1} (FWHM = 9 ± 0.1 cm^{-1}). We conclude that *p*-type InN NWs are strain-free and of high crystalline quality.

The piezoelectric properties of *p*-type InN NWs were first investigated using C-AFM, Fig. 3a. A Pt/Ir coated probe scans in contact mode across an array of as-grown NWs at a speed of 1 μm/s under a constant compressive force of 66.7 nN. The scan simultaneously captures both the topography of the NWs (top profile in Fig. 3b) and their corresponding piezoelectric current. The bottom profile in Fig. 3b presents a typical current output.

(a) (b)

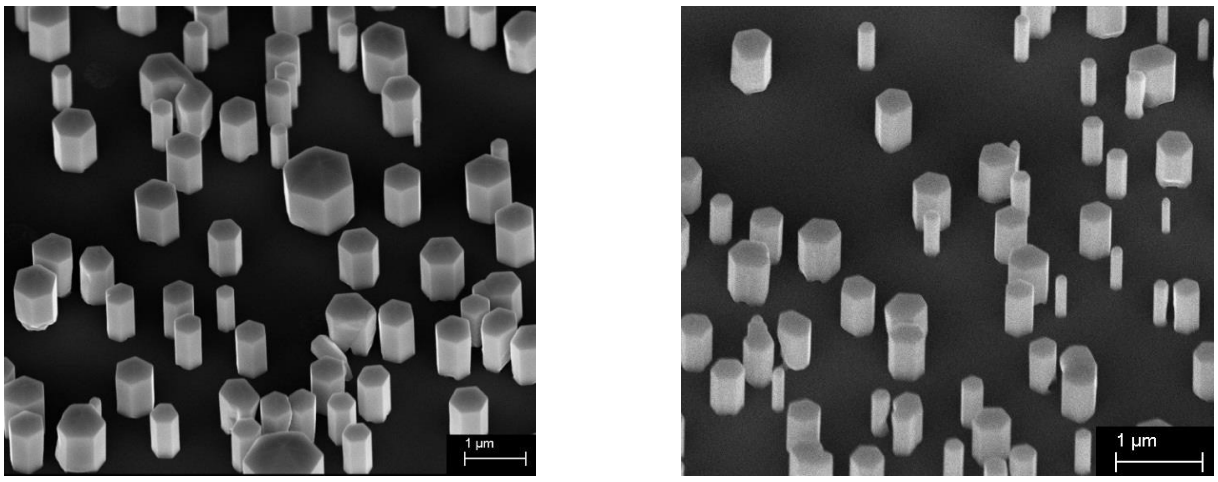

Fig. 1 SEM images of (a) *p*-type and (b) intrinsic InN NWs grown on Si (1 1 1) substrate, taken at a 45 °angle.

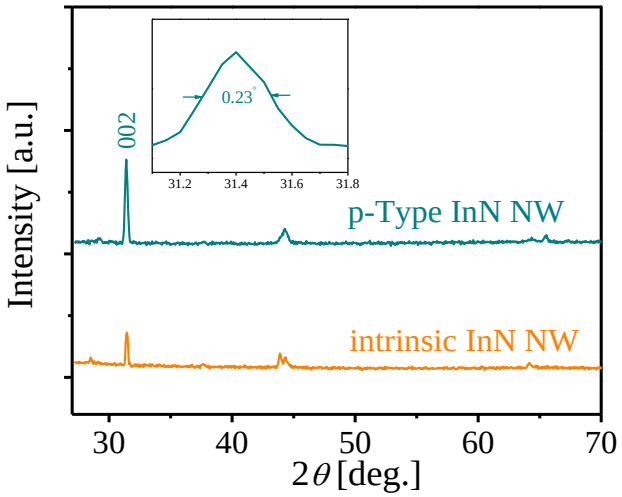

Fig. 2 The 2θ-scan spectra of the XRD intensity for p-type and intrinsic InN NWs, demonstrating the high crystalline quality of as-grown NWs on silicon substrate.

Current spikes of up to more than 300 pA occur at the leading edge of each nanowire along the AFM probe scanning direction (left to right). The electric current signal is roughly two orders of magnitude higher than the noise level in the C-AFM scan (~3 pA). This current arises due to the compressive load applied to individual NWs by the AFM tip.

The inset in Fig. 3b shows an AFM topography image of the NWs under test. The scan line is marked with a dashed line in the inset. The peaks in the topography profile, the upper curve in Fig. 3b, indicate that the NW heights are about 1.0 μm, consistent with the SEM images shown in Fig. 1a. The profile also indicates that the diameter of individual NWs is ~900 nm, which is much higher than that measured by SEM (~400 nm). This value is an artefact caused by the conic shape of the probe tip (cone angle 40 °) and the flexibility of the NWs. Contact typically occurs between the side face of the probe tip cone and the NW. As the probe continues to scan, it drags the wire with it. As the wire deforms, the probe tip climbs across the NW top and drags the NW along with it, until the tip leaves the NW top surface. The two consecutive spikes in the electric current profile on the right-hand side of Fig. 3b occur because two neighbouring nanowires in a row are in very close proximity, such that the topography profile is unable to distinguish them as two individual wires. They instead appear as a joint and broader peak.

The good correlation between the location of electric current spikes and the leading edge of the NWs indicates that the measured electric current is indeed generated by the InN NWs as they are compressed. For further confirmation, four experiments (Fig. S2†) were carried out to exclude the possibility that the output current arose from friction, contact potential, or other artefacts:

1) Similar C-AFM scans of a heavily doped Si film show no detectable current signals, which indicates that Si has no piezoelectric effect.[28] This is consistent with the noise floor results observed in the troughs of Fig. 3b where the tip contacts the Si substrate.

2) C-AFM scans of doped GaN NWs (highly conductive) produce no detectable current signals due to a screening effect, where the positive and negative charges generated piezoelectrically are completely compensated for by free charge carriers.[29, 30]

3) C-AFM scans of intrinsic GaN NWs lead to sharp output current spikes, attributable to the piezoelectric effect and similar to those reported in Fig. 3b.

4) C-AFM scans of *p*-type InN NWs with a bare Si tip detect no current signals because of Ohmic contact between the Si tip and the NW. Typically, a Schottky contact is needed to detect piezoelectric signals.

In summary, all observations support the conclusion that the electric current signals measured on *p*-type InN NWs originate from the NWs' piezoelectric effect.

Fig. 3c and e show three-dimensional images of the electric currents measured from *p*-type and intrinsic InN NWs in C-AFM over an area of 10 ×10 μm^2, respectively. Most of the current spikes from the *p*-type InN NWs are positive, with a maximum output current of 331 pA. Only a few negative current spikes

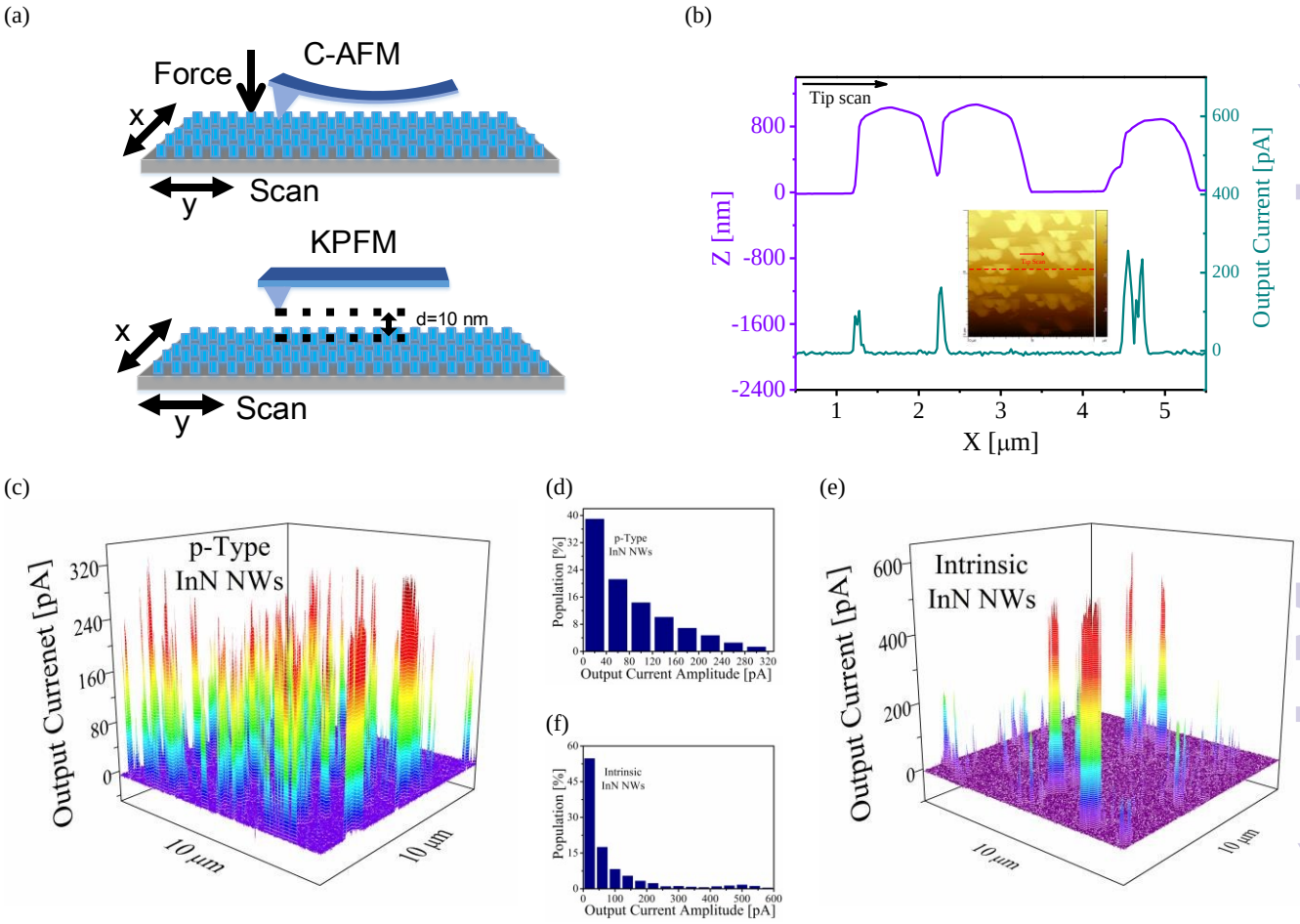

Fig. 3 Piezoelectric characteristics of InN NWs. (a) Schematic illustration of the experimental setup for C-AFM and KPFM scans. (b) Line profiles of t topography and output current of *p*-type InN NWs; the inset is an AFM image of the surface; (c) *p*-type and (e) intrinsic InN NWs' output current for a C-AFM of 10 μm × 10 μm area with a scan speed of 10 μm/s under a constant normal force of 66.7 nN; and the statistical distribution of (d) *p*-type and (f) intrinsic NW output current.

(less than 0.02% of the whole population) are observed exhibiting a smaller magnitude of -20.5 pA or less. Thus, the overall negative current output is negligible compared to the positive current output. Fig. 3d shows a histogram of the measured piezoelectric current. Quantitative analysis reveals that these NWs can produce an average output current density of 90.7 ± 70.6 pA over 100 μm^2 area. Four *p*-type InN NW samples were tested, producing similar results. For intrinsic NWs, the current spikes have large fluctuations, with a maximum output current of 600.9 pA, while most current spikes are below 50 pA. Fig. 3f shows a histogram of the measured piezoelectric current. The intrinsic NWs can produce an average output current density of 101.8 ± 127 pA over a 100 μm^2 area.

Assuming negligible capacitance, the NW output current I_s can be written as:[31]

$$I_s \approx V_s / (r_0 + r_c) \quad (1)$$

where V_s is the piezopotential generated by mechanical strain, r_0 is the resistance of the NWs, including the surface depletion effect,[32] and r_c is the contact resistance of the metal-semiconductor interface.[33] The large output current fluctuations for intrinsic NWs may indicate more diversified interface and surface effects.

A series of C-AFM scans were performed on the *p*-type InN NWs under identical experimental conditions apart from progressive changes in the compressive force applied to the AFM probe. As expected, the average piezoelectric current was roughly proportional to the applied force (Fig. 4a). At a force of 83 nN, the average piezoelectric current from the *p*-InN NWs ~ 93 pA.

Fig. 4b shows the electrical transport properties of InN NW The current-voltage (*I-V*) curves are obtained by engaging a conductive Pt/Ir AFM probe tip with individual NWs and using it as the top electrode. A compressive force of 66.7 nN is applied between the tip and the NW to establish and maintain a stable electric contact. The *I-V* measurements are performed by applying a bias voltage to the AFM probe and sweeping the voltage. The curves (Fig. 4b) show a clear asymmetric and rectifying behaviour, which can be ascribed to the Schottky contact formed between the Pt/Ir tip and InN NWs. The overall wire resistance ($r_c + r_0$) at 1.0 V is calculated as 14.2 MΩ for type and 13.0 MΩ for intrinsic NWs. We note that intrinsic InN

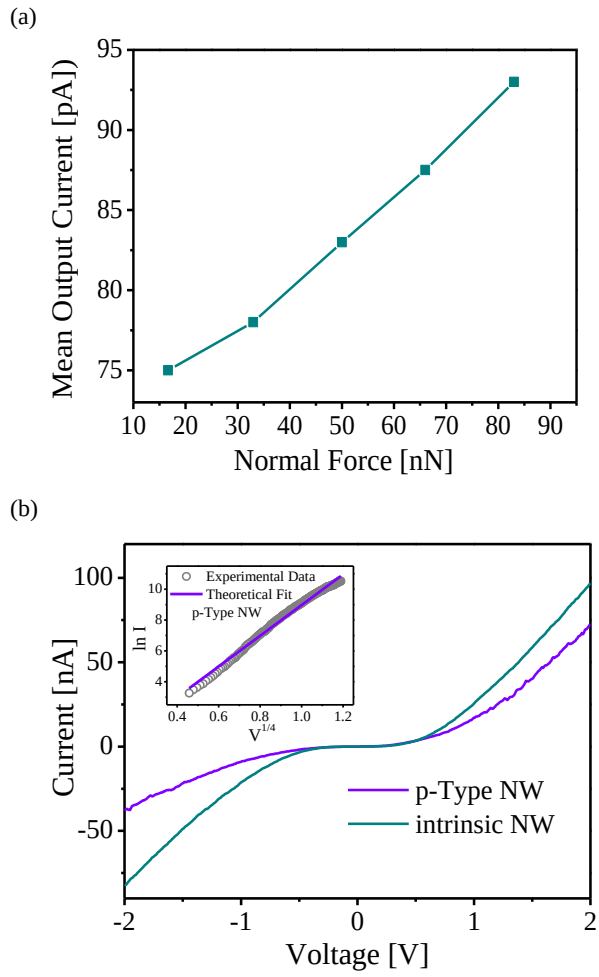

Fig. 4 (a) Measured output current as a function of the compressive force applied to *p*-type InN NWs; (b) Measured *I-V* curves for *p*-type and intrinsic InN NWs. The inset compares the *ln I* – $V^{1/4}$ curves for the thermionic emission-diffusion model and the experimental results for *p*-type InN NWs.

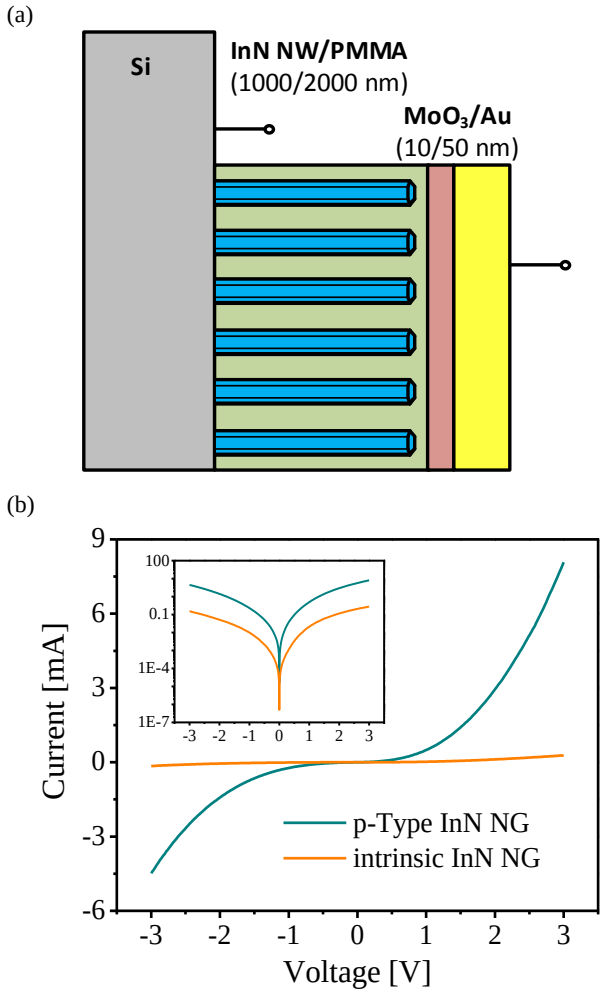

Fig. 5 (a) Schematic diagram of the InN NW-based NG. (b) The measured current-voltage curves of the *p*-type and intrinsic NGs at room temperature. The inset shows the Log_{10} *I-V* curves for the NGs.

NWs are effectively *n*-type doped due to the presence of surface states/defects.[34] Adding *p*-dopant would first compensate the trap states near conduction band edge, leading to a reduction of free charge carrier density. Relatively low *p*-doping level, together with the low hole mobility, compared to that of electrons, contribute to the relatively large resistance of the *p*-doped NWs. In addition, the longer length and smaller radius (smaller cross-section area) of the *p*-doped InN NWs (Fig. 1) may further contribute to higher resistance. An estimate of the voltage drop across individual NWs (V_s) can be found from Equation (1), by multiplying the measured NW current (I_s) by the overall NW resistance calculated from its *I-V* curve. Using this method, the ratio of V_s generated in intrinsic NWs to that generated in *p*-type NWs is found to be 1.03. Thus, the average piezoelectric properties of *p*-type and intrinsic InN NWs are similar.

To investigate the impact of Mg doping on the overall resistance of *p*-type InN NWs, transport behaviour across the interface between the NWs and the Pt/Ir AFM probe was modelled as a Schottky junction. This is described by the thermionic-emission-diffusion (*TED*) model.[35]

$$I_f = AA^{**}T^2 \exp(-\frac{\phi_B}{k_B T}) \exp(\frac{qV_f}{nk_B T} - 1)$$

$$V_f = \sqrt{\frac{qE_m}{4\pi\varepsilon_s}}, E_m = \sqrt{\frac{2qN}{\varepsilon_s}\left(V + V_{bi} - \frac{kT}{q}\right)} \quad (2)$$

where A is the area of the Schottky barrier, A^{**} is the effective Richardson constant, T is the temperature, ϕ_B is the Schottky barrier height (SBH), k_B is the Boltzmann constant, q is the electron charge, V_f is the voltage drop on the forward biased Schottky diode, N is the carrier concentration, and n is the ideality factor. The inset in Fig. 4b compares the experimental *lnI* – $V^{1/4}$ curve and the theoretical curve for *p*-type InN NWs. It shows excellent agreement between the model and experiment throughout the bias range.

The InN NWs samples were integrated into piezoelectric NGs (Fig. 5a and Fig. S3†). The electric characteristics of NGs based on *p*-type and intrinsic InN NWs are next investigated. Fig. 5b shows the measured *I-V* curves of the NGs. Similar to the *I-V* curves of individual NWs, they exhibit nonlinear characteristics, attributable to the Schottky-junction interface between the

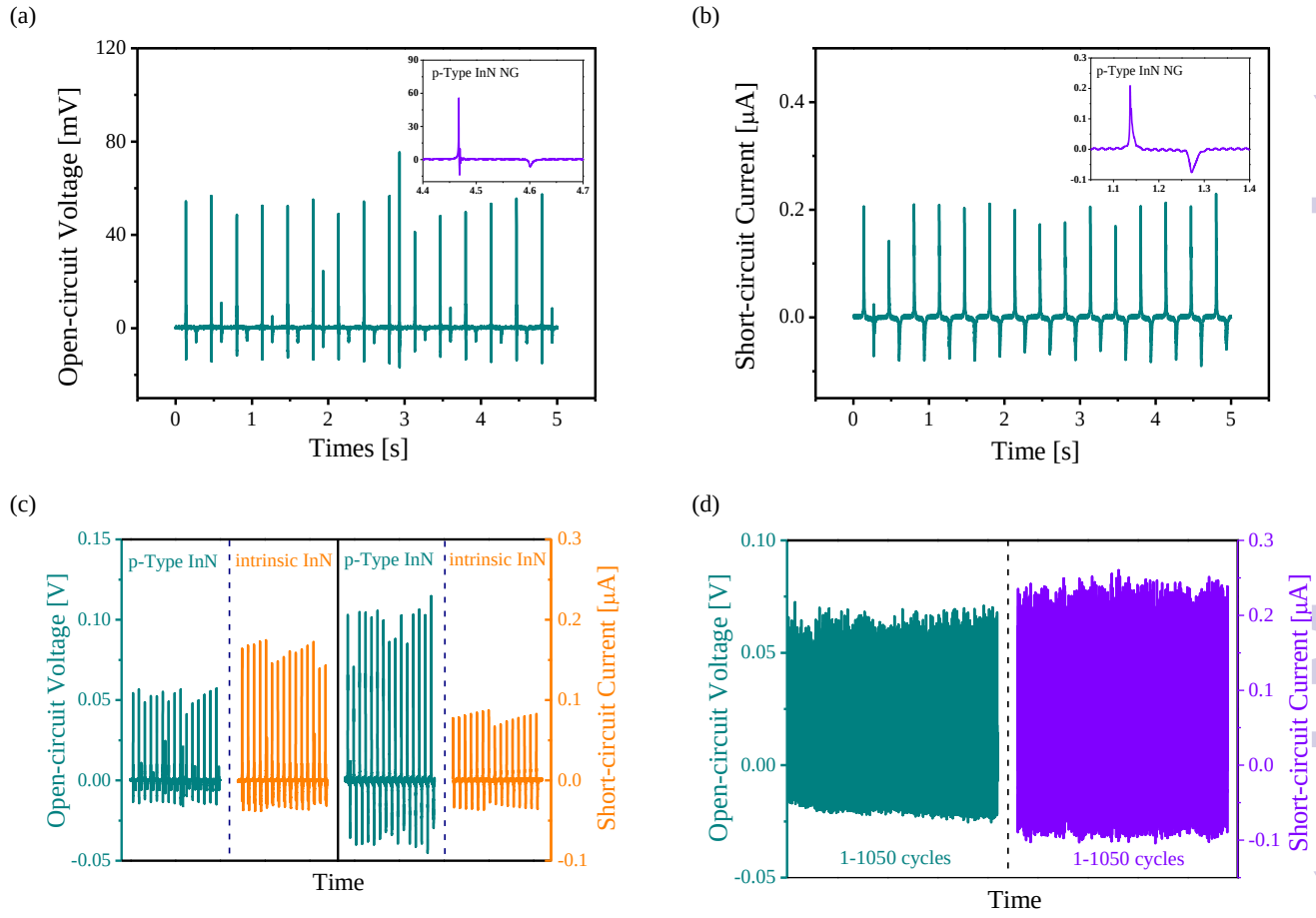

Fig. 6 Comparison of *p*-type and intrinsic InN NGs' performance at an acceleration amplitude of 2 m/s^2 and a frequency of 3 Hz. The measured (a) open-circuit voltage, average peak value of ~0.055 V, and (b) short-circuit current, average peak value of 211 nA, for *p*-type NGs. The insets show the signals from one cycle of mechanical vibration. (c) The measured open-circuit voltage and short-circuit current of *p*-type and intrinsic NGs. (d) Long-term *p*-type NGs open-circuit voltage V_{oc} and short-circuit current I_{sc} recorded over 1050 excitation cycles.

electrode (MoO_3/Au layer) and the InN semiconductor NWs. The *p*-type NG is more conductive than the intrinsic (*n*-doped) NG in both forward and reverse biases. The NGs' electric resistance at 1.0 V is calculated as R_i = 1 kΩ and 20 kΩ for *p*-type and intrinsic NGs, respectively. At 100 kHz, NG capacitances are measured as C_i = 0.589 and 0.582 nF, respectively (Fig. S4†). Although the *p*-type NG contains slight more high permittivity InN NWs than the intrinsic NG,[36] it also has a larger capacitive gap due to the longer *p*-type NWs. As a result, they end up with similar capacitance.

Fig. 6a and b present the *p*-type NGs' open-circuit voltage (V_{oc}) and short-circuit current (I_{sc}) output, respectively, under external dynamic strain. The NGs' substrate was anchored on a fixed stopper, leaving the top electrode facing outward and free standing. The shaker moved up and down, applying periodic strain to the NWs by striking the top electrode at the end of each cycle (Fig. S5†).[37, 38] The excitation frequency was set to 3 Hz, and the acceleration amplitude to 2 m/s^2. The NGs' response to individual mechanical strain cycles appears as a series of voltage or current spikes. The peak values of the output voltage and current exhibit reasonable consistency between pulses, with an average peak value of ~55 mV for V_{oc} and ~211 nA for I_{sc}. These values represent a potential maximum output power density of $(V_{oc} \times I_{sc})/A$ of ~0.012 μW/cm^2. The inset shows the open-circuit voltage V_{oc} and short-circuit current I_{sc} during a single loading-unloading cycle. Impact bounce is observed in V_{oc} output during the loading cycle, as the shaker head bounces on the NG's top electrode surface. It is not observed in I_{sc} because of the increase in the effective damping level once the circuit is closed.

Switching polarity tests were conducted to verify that the measured signals came from the piezoelectric response of the NG devices rather than from electromagnetic interference noise or other artefacts (Fig. S6c†). Switching polarity changed the sign of the measured open-circuit voltage V_{oc} and short-circuit current I_{sc}, but did not change their magnitudes or wave forms. The same experiments were performed on control devices with a layer structure similar to that of the NG devices but no InN NW layer. They showed no appreciable voltage or current spikes (Fig. S6d†), confirming that the electric signals from the NGs result from the InN NWs' piezoelectric response.

The *p*-type and intrinsic NGs were tested under the same experimental conditions to compare their performance. At a fixed external excitation with an acceleration amplitude of 2 m/s^2 and a frequency of 3 Hz, both NGs yielded substantial

Table I. Comparison of *p*-type and intrinsic NGs' performance.

	V_{oc} [V]	I_{sc} [uA]	$V_{oc} \times I_{sc}$ [nW]	R_i @ 1V [Ω]	C_i @ 100 kHz [nF]
p-type	0.055	0.211	11.6	1 k	0.589
intrinsic	0.085	0.08	6.8	20 k	0.582

piezoelectric response (Fig. 6c); nevertheless, their output differed greatly. The *p*-type NG's short-circuit current is 2.63 times that of the intrinsic NG, but it has a lower open-circuit voltage of 0.055 V compared to 0.085 V for the intrinsic NG. Table I shows that the power product ($V_{oc} \times I_{sc}$) of the *p*-type NG is 70% higher than that of the intrinsic NG.

The long-term stability of the InN nanowire-based NGs was next investigated. The *p*-type NG was tested for 1050 consecutive cycles. Strain was applied by an external excitation with an acceleration amplitude of 2 m/s^2 and a frequency of 3 Hz, and the open-circuit voltage and short-circuit current were recorded. The results, shown in Fig. 6d, are fairly consistent over the entire test span.

4. Discussion

4.1 Doping Improvement of NW Piezopotential

The NGs' working mechanism is based on coupled piezoelectric and semiconducting properties. Once stress is applied to the top electrode, the piezoelectric effect creates fixed charges close to the NWs' end surfaces, resulting in a macroscopic potential across the length of the NWs. An important limitation of piezoelectric semiconductor NWs is that holes and free electrons present in the NWs can greatly reduce this piezopotential via a screening effect.[39] To investigate this effect in InN NWs, the piezopotential profile inside NWs with different doping concentrations was simulated using the TiberCAD multiscale simulation tool.[40, 41] For simplicity, the simulations were restricted to steady-state conditions under thermal equilibrium, at a temperature of 300 K. Fig. 7a and b show the potential along the *c*-axis of 1.0 μm *p*-type and intrinsic (*n*-type) InN NWs when subjected to compressive force of 100 nN. Clearly, the higher the carrier concentration, the lower the magnitude of the piezopotential, thus the more pronounced is piezoelectric screening due to free carriers. A finding consistent with result for individual ZnO NWs.[40-42] The use of low concentration *p*-type doping to balance the free electrons in intrinsic InN NWs reduces the screening effect and increases the piezopotential of *p*-type InN NWs beyond that realized in intrinsic InN NWs.

In our experiments, it was found that the average piezopotential of *p*-type and intrinsic InN NWs were similar, as shown in Fig. 3c and d. This might be attributed to the fact that the effective free charge carrier density in the *p*-type NWs (estimated in the range of 2×10^{15} to 6×10^{15} cm^{-3}) [25] is somehow comparable to that in the intrinsic NWs (effective *n*-type concentration of ~ 4×10^{15}cm^{-3}) [19].

4.2 Scatter of NW Piezopotential

Although the observed maximum piezoelectric current from the intrinsic NWs (601 pA) is much higher than that of the *p*-type NWs (331 pA), on average their piezoelectric current from NW ensembles over an area of 100 μm^2 are comparable, i.e., 101 ± 127 pA for intrinsic NWs and 90.7 ± 70.6 pA for *p*-type NWs. Furthermore, the piezoelectric current from the intrinsic NWs exhibits a much larger scattering than the *p*-type NWs. The observed higher maximum piezoelectric current suggests that intrinsic NWs are potentially a better candidate for NG application. Nevertheless, the larger divergence in the piezoelectric current yields a poorer overall device performance for intrinsic InN NGs comparing to *p*-type NGs. This scatter may be attributed to their higher vulnerability to unstable surface states.

InN surfaces are known to possess a high concentration of donor-type surface states, resulting in an electron accumulation layer,[10, 43, 44] which may lead to an elevated surface potential. Using non-contact KPFM, the electrical potential difference between the conductive probe tip and the sample surface provides a measure of the NWs' surface potentials. Fig. 8a and b

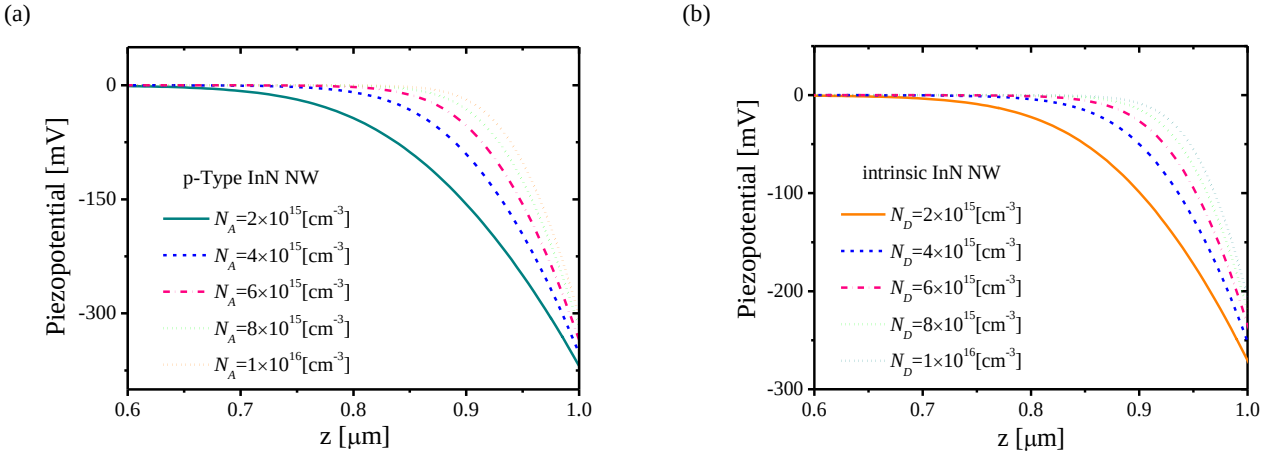

Fig. 7 Calculated piezopotential in (a) *p*-type and (b) intrinsic (*n*-type) InN NW ($D = 200\ nm$ and $L = 1\ \mu m$) surrounded by free space and subject to a compressive force of 100 nN.

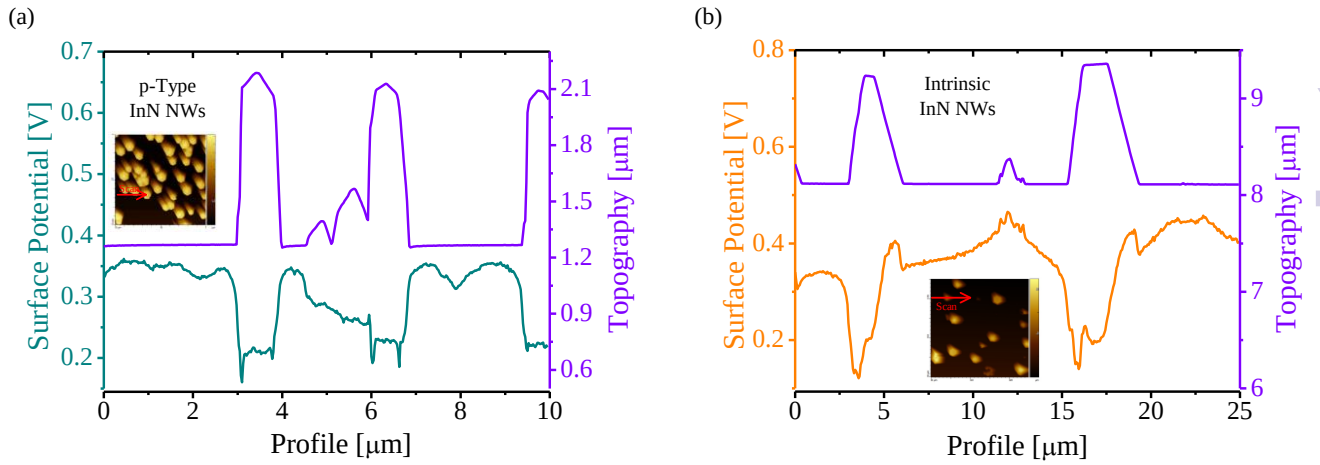

Fig. 8 Surface potential (bottom) and topography (top) profiles during a line scan of (a) *p*-Type; (b) intrinsic InN NWs.

show the topography and surface potential measured along a line during a raster scan of 10 × 10 μm^2 of *p*-type and 25 × 25 μm^2 of intrinsic InN NWs. The *p*-type NWs show a potential difference of up to -160 mV (scan area average -141 ± 11 mV) between the NWs and their surroundings. For intrinsic NWs, the potential difference is higher, reaching a maximum of -290 mV (scan area average - 236 ± 26 mV). These measurements were repeated on 10 separate areas. While some variability was observed in the measured surface potential, they all show that *p*-type NWs' surface potential difference is much lower than intrinsic NWs. We propose that the elevated surface potential of intrinsic NWs increases the instability of their surface states and, therefore, the variability of their piezoelectric properties.

4.3 NG Performance

To analyse the performance of the NGs, we note that their current may be approximated as

$$I = \frac{V}{|Z|} \tag{3}$$

where V is the voltage drop across the NG electrodes, and $|Z|$ is the magnitude of its total internal impedance. Since the NGs' inductance is negligible, impedance Z consists of a resistive component $Z_r = R_i$ and a capacitive component $Z_c = (i\omega C_i)^{-1}$ connected in parallel, where ω is the angular frequency.[45] Therefore, the magnitude of the total internal impedance is

$$|Z| = \frac{R_i}{\sqrt{1 + (R_i \omega C_i)^2}} \tag{4}$$

Calculating the electric resistance at 1 V from Fig. 3b, measuring the capacitance at 100 kHz (Table I), and using Equation (4), the impedance ratio of the intrinsic to *p*-type NGs is ~2.89. Assuming similar piezoelectric performance for the *p*-type and intrinsic NGs would suggest a similar open-circuit voltage ratio. The measured ratio of the intrinsic to the *p*-type NGs' open-circuit voltage V_{oc} is 1.55. The lower V_{oc} ratio reflects better piezoelectric conversion efficiency of *p*-type NGs due to the smaller diameter of *p*-type NWs compared to intrinsic NWs.[36]

Similarly, Equation (3) suggests that the short-circuit current of a *p*-type NG should be 2.89 times that of the intrinsic NG. The actual ratio of the short-circuit current is 2.64 (Table I), which is in fair agreement with the estimated value. The driving factor for the significant difference between *p*-type and intrinsic NGs' impedance and short-circuit current is the lower electrostatic losses in *p*-type NGs due to longer and narrower NWs and a higher fill ratio β_p.

5. Conclusions

We have successfully fabricated the first piezoelectric NG based on InN NWs. Raman spectroscopy, XRD, C-AFM, and KPFM were used to characterize *p*-type and intrinsic InN NWs. The statistical distribution of their piezopotential, when compressed by an AFM tip, was also measured. While intrinsic NWs demonstrate the possibility for a much higher piezoelectric response than *p*-type NWs, this prospect is undermined by their highly scattered and inconsistent responses across the array. On the other hand, even though *p*-type NWs have lower peak piezopotential, their more consistent response results in average piezoelectric performance similar to that of intrinsic NW arrays.

We propose that the variability in intrinsic NWs' response is due to higher instability of surface charge levels than *p*-type NWs. This suggests that the surface passivation of intrinsic NWs may improve their performance. On the other hand, the piezopotential of *p*-type NWs can be significantly improved beyond that realized here by lowing the *p*-type carrier concentration to reduce free carriers in the NWs and their detrimental screening effect.

The power product of *p*-type NGs was 70% more, at 11.6 nW, than the power product of intrinsic NGs. Both types of NGs had an area of 0.81 cm^2 and were excited by an acceleration amplitude of 2 m/s^2 and frequency of 3 Hz. The *p*-type NGs had 160% more short-circuit output current, at I_{sc} = 211 nA, than intrinsic NGs. The higher output power of the *p*-type reflects better piezoelectric energy conversion efficiency than intrinsic NGs. The higher output current of *p*-type NGs reflects a much lower impedance than intrinsic NGs. Both results were due to

lower electrostatic losses in *p*-type NGs enabled by a more advantageous NW morphology, longer and narrower NWs and increased NW area density, resulting from Mg doping. In addition, the higher surface charge levels of intrinsic InN NWs appear to play a role the elevated resistance of intrinsic NGs.

Acknowledgements

The authors thank Karim EI-Rayes and Man Chun Tam for valuable discussions and technical assistance. We acknowledge financial support from the Natural Science and Engineering Research Council (NSERC) of Canada, the Canadian Foundation of Innovation (CFI), the CMC Microsystems, and the Ontario Research Fund (ORF). RH acknowledges WIN Graduate Fellowship.

References

1 Z. L. Wang, *Nano Today*, 2010, **5**, 512-514.
2 Y. Qi and M. C. McAlpine, *Energy Environ. Sci.*, 2010, **3**, 1275-1285.
3 A. I. Hochbaum and P. Yang, *Chemical Reviews*, 2010, **110**, 527-546.
4 Y. Qiu, H. Zhang, L. Hu, D. Yang, L. Wang, B. Wang, J. Ji, G. Liu, X. Liu and J. Lin, *Nanoscale*, 2012, **4**, 6568-6573.
5 Z. L. Wang, *Adv. Mater.*, 2012, **24**, 4632-4646.
6 T. I. Lee, S. Lee, E. Lee, S. Sohn, Y. Lee, S. Lee, G. Moon, D. Kim, Y. S. Kim and J. M. Myoung, *Adv. Mater.*, 2013, **25**, 2920-2925.
7 X. Wang, J. Song, F. Zhang, C. He, Z. Hu and Z. Wang, *Adv. Mater.*, 2010, **22**, 2155-2158.
8 C. T. Huang, J. Song, C. M. Tsai, W. F. Lee, D. H. Lien, Z. Gao, Y. Hao, L. J. Chen and Z. L. Wang, *Adv. Mater.*, 2010, **22**, 4008-4013.
9 C.-T. Huang, J. Song, W.-F. Lee, Y. Ding, Z. Gao, Y. Hao, L.-J. Chen and Z. L. Wang, *J. Am. Chem. Soc.*, 2010, **132**, 4766-4771.
10 N. J. Ku, C. H. Wang, J. H. Huang, H. C. Fang, P. C. Huang and C. P. Liu, *Adv. Mater.*, 2013, **25**, 861-866.
11 A. G. Bhuiyan, A. Hashimoto and A. Yamamoto, *J. Appl. Phys.*, 2003, **94**, 2779-2808.
12 T. Matsuoka, H. Okamoto, M. Nakao, H. Harima and E. Kurimoto, *Appl. Phys. Lett.*, 2002, **81**, 1246-1248.
13 J. Wu, W. Walukiewicz, K. Yu, J. Ager Iii, E. Haller, H. Lu, W. J. Schaff, Y. Saito and Y. Nanishi, *Appl. Phys. Lett.*, 2002, **80**, 3967-3969.
14 J. Wu, W. Walukiewicz, W. Shan, K. Yu, J. Ager III, E. Haller, H. Lu and W. J. Schaff, *Phys. Rev. B*, 2002, **66**, 201403.
15 Y.-L. Chang, F. Li, A. Fatehi and Z. Mi, *Nanotechnology*, 2009, **20**, 345203.
16 Y. L. Chang, Z. Mi and F. Li, *Adv. Funct. Mater.*, 2010, **20**, 4146-4151.
17 S. Zhao, Q. Wang, Z. Mi, S. Fathololoumi, T. Gonzalez and M. Andrews, *Nanotechnology*, 2012, **23**, 415706.
18 S. Zhao, Z. Mi, M. Kibria, Q. Li and G. Wang, *Phys. Rev. B*, 2012, **85**, 245313.
19 S. Zhao, S. Fathololoumi, K. Bevan, D. Liu, M. Kibria, Q. Li, G. Wang, H. Guo and Z. Mi, *Nano Lett.*, 2012, **12**, 2877-2882.
20 M. Holtz, I. Gherasoiu, V. Kuryatkov, S. Nikishin, A. Bernu[illegible] and M. Holtz, *J. Appl. Phys.*, 2009, **105**, 3702.
21 V. Polyakov, F. Schwierz, F. Fuchs, J. Furthmüller and F. Bechstedt, *Appl. Phys. Lett.*, 2009, **94**, 022102.
22 F. Glas, *Phys. Rev. B*, 2006, **74**, 121302.
23 H. Xiang, S.-H. Wei, J. L. Da Silva and J. Li, *Phys. Rev. B*, 2008, **78**, 193301.
24 M. Knelangen, V. Consonni, A. Trampert and H. Riechert, *Nanotechnology*, 2010, **21**, 245705.
25 S. Zhao, B. Le, D. Liu, X. Liu, M. Kibria, T. Szkopek, H. Guo and Z. Mi, *Nano letters*, 2013, **13**, 5509-5513.
26 S. Lee, S. H. Bae, L. Lin, Y. Yang, C. Park, S. W. Kim, S. N. Cha, H. Kim, Y. J. Park and Z. L. Wang, *Adv. Funct. Mater.*, 2013, **23**, 2445-2449.
27 G. Zhu, A. C. Wang, Y. Liu, Y. Zhou and Z. L. Wang, *Nano Lett.*, 2012, **12**, 3086-3090.
28 Z. L. Wang, *Adv. Mater.*, 2009, **21**, 1311-1315.
29 C. H. Wang, W. S. Liao, Z. H. Lin, N. J. Ku, Y. C. Li, Y. C. Chen, Z. L. Wang and C. P. Liu, *Adv. Energy Mater.*, 2014, [illegible]
30 C. H. Wang, W. S. Liao, N. J. Ku, Y. C. Li, Y. C. Chen, L. W. Tu and C. P. Liu, *Small*, 2014, **10**, 4718-4725.
31 J. Liu, P. Fei, J. Zhou, R. Tummala and Z. L. Wang, *Appl. Phys. Lett.*, 2008, **92**, 173105.
32 B. Simpkins, M. Mastro, C. Eddy Jr and P. Pehrsson, *J. Appl. Phys.*, 2008, **103**, 104313.
33 S. Lee, R. Hinchet, Y. Lee, Y. Yang, Z. H. Lin, G. Ardila, L. Montès, M. Mouis and Z. L. Wang, *Adv. Funct. Mater.*, 2014, **24**, 1163-1168.
34 S. Zhao, O. Salehzadeh, S. Alagha, K. Kavanagh, S. Watkins and Z. Mi, *Appl. Phys. Lett.*, 2013, **102**, 073102.
35 D. K. Schroder, *Semiconductor material and device characterization*, John Wiley & Sons, 2006.
36 R. Hinchet, S. Lee, G. Ardila, L. Montès, M. Mouis and Z. L. Wang, *Adv. Funct. Mater.*, 2014, **24**, 971-977.
37 L. Lin, Q. Jing, Y. Zhang, Y. Hu, S. Wang, Y. Bando, R. Yu, J. Han and Z. L. Wang, *Energy Environ. Sci.*, 2013, **6**, 1164-1169.
38 G. Liu, E. Abdel-Rahman and D. Ban, *J. Appl. Phys.*, 2015, **118**, 094307.
39 K. Y. Lee, B. Kumar, J.-S. Seo, K.-H. Kim, J. I. Sohn, S. N. Cha, D. Choi, Z. L. Wang and S.-W. Kim, *Nano Lett.*, 2012, **12**, 1959-1964.
40 R. Araneo, G. Lovat, P. Burghignoli and C. Falconi, *Adv. Mater.*, 2012, **24**, 4719-4724.
41 G. Romano, G. Mantini, A. Di Carlo, A. D'Amico, C. Falconi and Z. L. Wang, *Nanotechnology*, 2011, **22**, 465401.
42 Y. Gao and Z. L. Wang, *Nano Lett.*, 2009, **9**, 1103-1110.
43 E. Halpern, G. Elias, A. Kretinin, H. Shtrikman and Y. Rosenwaks, *Appl. Phys. Lett.*, 2012, **100**, 262105.
44 N.-J. Ku, J.-H. Huang, C.-H. Wang, H.-C. Fang and C.-P. Liu, *Nano Lett.*, 2012, **12**, 562-568.
45 F. F. Comjani, U. Willer, S. Kontermann and W. Schade, *Appl. Phys. Lett.*, 2014, **104**, 143113.